

## Experimental observations of methane–oxygen diffusion flame structure in a sub-millimetre microburner

C. MIESSE,<sup>†</sup> R. I. MASEL,<sup>\*†</sup> M. SHORT<sup>‡</sup> and M. A. SHANNON<sup>§</sup>

<sup>†</sup>Department of Chemical and Biomolecular Engineering, University of Illinois, Urbana, IL 61801, USA

<sup>‡</sup>Department of Theoretical and Applied Mechanics, University of Illinois, Urbana, IL 61801, USA

<sup>§</sup>Department of Mechanical and Industrial Engineering, University of Illinois, Urbana, IL 61801, USA

(Received 6 October 2003; in final form 9 September 2004)

We examine the structure of confined, laminar methane–oxygen diffusion flames in an alumina microburner with a sub-millimetre dimension. To minimize termination of gas-phase combustion via surface radical quenching, the reactor walls are chemically treated and annealed. We show, through chemiluminescent images, that gas-phase methane–oxygen diffusion flames exist in the microburner without the need for catalytic reaction. However, their structure differs from the continuous laminar diffusion flame profiles that we would expect in a similar burner configuration on a macroscopic scale. Instead, we observe a sequence of isolated reaction zones structures (flame cells) that form along the length of the microburner combustion channel aligned in the direction of the gas flow. This form of cellular diffusion flame instability appears to be unique to wall-confined combustion in microscale devices. The number of flame cells observed depends on the inlet gas velocities and initial mixture strengths.

### 1. Introduction

Since Davy [1] demonstrated that flames are quenched on trying to pass through a fine wire gauze, it has been widely shown that the gas-phase combustion of hydrocarbon fuels at atmospheric pressures cannot generally be sustained below a critical reactor dimension, usually of the order of a few millimetres for hydrocarbon/air reactions [1, 2]. In spite of this, the high energy density appeal of hydrocarbon fuels, compared with lithium ion batteries for example, has initiated much research in using microcombustion devices as power sources in micromechanical systems such as microengines (e.g. internal combustion engines [4–7] and gas turbines [8]), as heat sources for microfuel reformers, or as an integral part of a flame ionization detector in portable chemical and biological detectors. This is an area known as micropower generation (MPG), and a review of some of these MPG devices can be found in [9]. In practice, these devices require combustion to occur in vessels with a critical dimension(s) less than the standard flame quenching distance for a given mixture. In order to achieve this, procedures and designs must be implemented that overcome the interfacial phenomena of flame quenching by both wall heat loss and vessel wall radical destruction, which become

---

\*Corresponding author. E-mail: r-masel@uiuc.edu

prominent as the combustion vessel decreases in size and the surface area to volume ratio increases. Thus many of the MPG devices that have been designed or proposed so far achieve stable heat generation by employing complex thermal management techniques and/or hydrocarbon fuel conversion via catalytic combustion. Primary examples include the single-pass counterflow heat exchanger/combustor [10] and the three-dimensional toroidal ‘Swiss Roll’ counterflow heat exchanger/combustor [11, 12].

To take advantage of the increase in the characteristic surface area to volume ratio as the vessel dimensions are reduced, a number of microcombustion systems utilize surface catalytic combustion [9]. One of the main drawbacks of this approach is that the combustion temperatures generated are significantly lower than those that can be obtained via gas-phase combustion, and consequently are not as useful as heat sources for microfuel reformers. In contrast to the catalytic combustion based approaches, the microburner (combustor) system described here supports gas-phase reaction in a microvessel constructed from alpha-phase polycrystalline alumina with a relatively conventional design configuration (figure 1). During combustion, the outside wall temperatures of the microburner can exceed 1500 K. Consequently, the integration of this microcombustor design with a microreactor could result in orders of magnitude increases in reaction rates as well as many orders of magnitude improvements in equilibrium constants for highly endothermic reforming reactions often considered for microreactors [13, 14], as compared to the catalytic microcombustor devices that operate at lower temperatures.

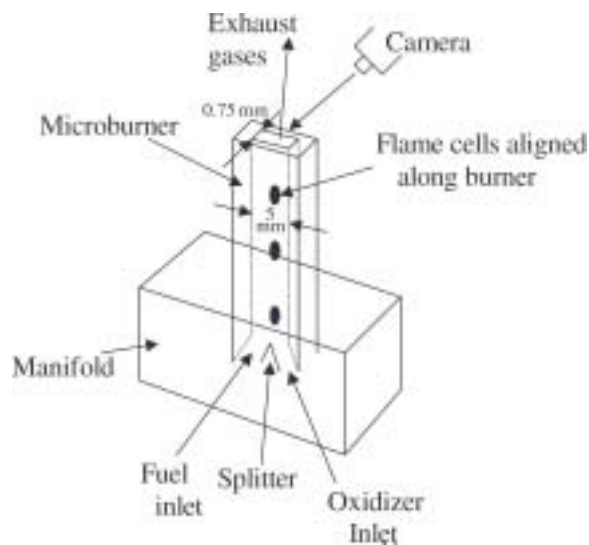
Much of the current emphasis in microcombustion technology is on the practical production of thermal energy for a micropower device. Thus far, comparatively little attention has been paid to the fundamental properties of the structure, properties and dynamics of spatially confined combustion at the microscale level. The purpose of this paper is to provide an insight into the novel flame structures that arise in gas-phase microburners. The microburner configuration discussed in the current work is shown in figure 1. The combustion channel has a straight rectangular geometry and is fed by two angled inlet gas supply legs as shown. The results shown here are for the non-premixed combustion of methane and oxygen in a microburner channel with a width of 0.75 mm (figure 1(b)). Gas-phase combustion in the combustion channel can only be sustained after the interior vessel walls have been chemically treated, annealed and then oxygen baked.

Although quenching distances for methane/oxygen combustion have been reported to be as low as 0.3 mm [2], in practice these are for a specific set of circumstances, e.g. for premixed flame propagation through parallel plates after direct initiation of the flame. In reality, the quenching distances depend intimately on many issues, including the nature of the reaction geometry, the temperature and material of the bounding walls, the surface preparation, and whether or not the reaction is completely confined within the bounding walls. For instance, Jensen [15] has examined the quenching distances of a premixed methane/oxygen torch flame between parallel plates of stainless steel, quartz and alumina. The temperature on the interior surface of the plates was controlled by a heat source or sink mounted on the outside of the plates. When this temperature was maintained below 500 K, the quenching distances were in the range 2–3 mm and did not vary significantly with the plate material. However, when the interior surface temperature was maintained close to 1000 K, the quenching distance was a strong function of plate composition. Of the three materials mentioned, alumina gave the shortest quenching distance (0.7 mm) and stainless steel the longest (1.8 mm). The implication is that at the lower wall temperatures, the dominant quenching mechanism is thermal, while at the higher temperatures it is related to the microscopic wall material structure and consequently to the relative degree of surface chemical reactions that occur.

In the current alumina microburner, the surface walls were treated, as described below, to minimize quenching of intermediate combustion reactants on the vessel walls. This procedure



(a)



(b)

Figure 1. (a) An image of one section of the Y-shaped alumina burner. (b) A 3D schematic drawing of final burner assembly. The section shown in (a) is joined with a second section with an identical cross-section pattern. This is mounted in a gas feed manifold. Fuel and oxidizer are supplied at the base of the burner, where the inlet streams are separated by a wedge-shaped splitter. The chemiluminescent images of the flame structure are taken by positioning a camera at the top of the burner in the exhaust stream, and angling it to one side, so that the length of the combustion channel can be observed.

enables the microburner to sustain gas-phase combustion with a sub-millimetre gap dimension. To give some indication of the success of this procedure, a microburner with the same configuration as that shown in figure 1, but with a gap dimension of 1 mm and no surface treatment, will not support any gas-phase methane–oxygen combustion. If chemically treated

and annealed, but with no oxygen bake, gas-phase combustion can be supported. For the 0.75 mm wide burner described here, gas-phase combustion can only be supported with both the annealing and oxygen bake. No further treatments are necessary to support combustion in a 0.5 mm burner. Currently, a 0.25 mm wide burner is being investigated.

With the geometry shown in figure 1 on a larger scale, we nominally would expect to see the flame structure comprising a premixed edge-flame either attached, or lifted, from the wedge-shaped splitter, trailing a continuous laminar diffusion flame. In contrast to this expected structure, in our sub-millimetre scale burner and for a supply of methane/oxygen, we instead observed multiple isolated reacting zones such as that schematically shown in figure 1. Presumably, these cells result from a cellular instability of the underlying laminar diffusion flame, but one that occurs along the length of the channel and aligned with the flow direction. The flame cells are extremely robust in nature, existing for a wide range of inlet velocities and initial mixture strengths. The number of flame cells is dependent on the initial supply conditions, varying between one and four for the length of the burners used here.

Of course, isolated multiple-flame structures have been observed previously, but for conditions different from those under consideration here. For instance, near-spherical premixed flame balls have been found to occur in premixed combustible mixtures in microgravity [16]. Isolated flame-string patterns have also been created by the break-up of a laminar edge-flame in a premixed or non-premixed counterflow in regions of high-strain flow [17]. Importantly, these structures only occur for fuel/oxidizer components with a sufficiently low Lewis number and in a combustion regime that is either near or below the one-dimensional extinction (or flammability) limit [18–20]. The appearance of cellular diffusion flame instabilities on a variety of burners is also well documented. The most relevant to our configuration is the 2D Wolfhard–Parker slot jet burner [21, 22]. These instabilities either occur as a wrinkling at the base of the flame sheet near the splitter, or as a series of distinct cells formed transverse to the flow direction along the flame sheet. No isolated cells were ever observed in the direction of the flow. Again though, the instability was only observed to occur in near-extinction conditions, either low Damköhler number or heat loss induced, and when the more completely consumed reactant has a Lewis number sufficiently less than unity. Note that such transverse instabilities would likely be suppressed in our burner due to the narrow transverse dimension of the channel (0.75 mm). Recent theoretical analyses [23, 24] have shown that the conditions required for the onset of cellular diffusion flame instabilities are consistent with these experimental observations. In contrast, the microcombustion flame cell structures observed here occur for a methane–oxygen reaction and in conditions that are not necessarily near limit.

Section 2 of this paper details burner manufacture and configuration. In section 3, we present a series of direct luminosity photographs of the emission from the methane–oxygen flame structures that were found in the sub-millimetre microburner for various supply conditions. Some of the mechanisms that may influence the creation of the flame cells are discussed in section 4.

## 2. Burner manufacture and configuration

The microburner is made from alpha-phase polycrystalline alumina, a material that is mechanically stable to 1800°C, with a melting point of 2050°C. Furthermore, it does not chemically degrade in a high-temperature atmosphere (below 1800°C) of oxygen and water vapour (present in large volumes in hydrocarbon reactions), as do many other ceramic materials at high temperatures, such as SiC. A procedure, described below, has been developed to maximize the resistance of the polycrystalline alumina surfaces to chemical quenching of combustion reactants, in particular OH radicals.

The burner was constructed by machining a 5 mm wide, 0.25 mm deep Y-shaped slot in a 40 mm × 10 mm × 1 mm polycrystalline alumina slide. A 0.5 mm deep Y-shaped channel was machined into a second slide. An image of one of the sections of the burner is shown in figure 1(a). Following machining, the surfaces of the alumina slides were treated using a three-step process developed to produce chemically inert surfaces on the reactor walls. First, to remove ionic and heavy metal contaminants from the surface, the slides were held at 80°C for ten minutes in a bath of deionized water, concentrated hydrochloric acid and 30% hydrogen peroxide at a 6:1:1 volume ratio. Slides were then annealed in an atmospheric environment at 1550°C for one hour to reduce the existence of grain boundaries and other surface imperfections that would serve as quenching sites for radicals. Before the final surface preparation technique, the machined faces of the slides (see figure 1(a)) were joined to form the microburner combustion channel and sealed with an alumina-based adhesive. The microburner was then mounted in a gas feed manifold made of alumina (figure 1(b)). The manifold supplies gases to either inlet of the inverted-Y mixing channel, and has dimensions of 1 1/2 in (length), 5/8 in (width) and 15/16 in (depth). The cavity into which the burner is mounted has dimensions of 13 mm (length), 5 mm (width) and 16 mm (depth). The bottom 13 mm of the burner typically sits in the manifold. A three-dimensional schematic of the final burner assembly is shown in figure 1(b). (In recent burner designs the manifold has been eliminated and the inlet leg sections extended away from the combustion channel. The resulting flame structures observed were the same in either case.) The microburner and manifold assembly were then heated to 1000°C for 12 hours via resistive heating while oxygen was fed to the reaction chamber. This final step acts to further passivate the microcombustor's surface, leaving it highly intolerable to reducing the potential for heterogeneous combustion reactions. Finally, the microburner was wrapped in fibrous alumina insulation to provide additional thermal insulation, although it should be noted that the burner would operate in a similar fashion in atmospheric air without the insulation. Current work is underway that will provide a more effective means of thermally insulating the burner from the exterior wall losses.

We studied the non-premixed reaction of methane with oxygen in the microburner. Methane safety is covered under UN code No. 3167, and EU code No. 601-001-00-4 and EC safety phrases S9 S16 S33. Compressed oxygen is covered under EC safety phrase S17. As shown in figure 1, methane was fed into one leg of the inverted-Y microburner, while oxygen was fed to the other. The inlet streams are separated by a wedge-shaped splitter, as seen at the bottom of the burner in figure 1(a). The methane and oxygen streams meet and react in the straight section of the inverted-Y section, while products and unreacted supply gases are exhausted out of the top of the burner into atmospheric air (figure 1(b)). The flame structures inside the burner were observed with chemiluminescent images taken with a Canon Powershot G1 camera and an IR cut filter lens. The camera was positioned directly over the top of the burner near the exhaust stream and angled to one side to view the flame structure that appears down the length of the burner, as indicated in figure 1(b). In the luminosity images taken in this way (shown below in figure 3), the flame cell near the bottom of burner, i.e. closest to the fuel/oxygen inlet, appears at the bottom of the images.

In many cases, the degree of fuel conversion in the burner is sufficiently incomplete (in many cases, gas chromatography measurements of the exhaust gases indicate that the methane conversion rate is less than 40%) that the unconsumed methane in the exhaust gases can mix with atmospheric air and, when ignited, results in an unconfined cone-shaped methane-air diffusion flame attached to the methane inlet side of the burner exit. Obviously, for practical applications, all the combustion must be confined to the microburner surfaces. In most cases, this flame may be extinguished by gently blowing over the top of the burner leaving the flame structure inside the burner unaltered. In other cases, the presence of the methane-air flame at the channel exit has some interesting consequences that are explored below.

For the results described below, the injection rates are given in terms of sccm units and an estimate of the Reynolds number ( $Re$ ). The standard volumetric flow rate was determined by mass flow rate controllers external to the burner assembly. It is difficult to give a precise value of the average injection velocity into the combustion chamber, since we do not know the temperature of the gases at the inlet. Reynolds number estimates were based on the total inlet velocity of fuel and oxidizer and on a gas with properties of an equimolar composition of methane and oxygen at 25°C and a channel diameter of 0.75 mm. The approximate Lewis numbers of undiluted methane and oxygen were taken to 0.95–1 and 1.05–1.1, respectively, in air.

Cold flow visualizations of the flow fields for the present microburner design were also conducted. Our primary concern was to establish whether the burner configuration could induce any hydrodynamic flow instabilities, such as Kelvin–Helmholtz vortical instabilities (due to the typical velocity difference in the inlet streams) or boundary layer separation due to the sharp corners near the inlet, which may influence or underlie the formation of the flame structures observed below. The visualization was performed by illuminating smoke particles injected into the supply stream within a thin sheet of 632.8 nm light from a He–Ne 8 mW laser shone through the top of the burner, in which one of the alumina surfaces was replaced by quartz. For the range of inlet gas velocities considered, the cold flow field is perfectly laminar. There is a counterflow field near the inlet where the angled inlet streams meet: the fluid is then turned toward the exit and proceeds straight down the combustion channel. A typical streamline indicating the flow field near the region of the mixing plane between inlet gases with flow rates of 100 sccm  $N_2$  and 200 sccm  $N_2$  ( $Re = 86$ ) is shown in figure 2.

### 3. Results

In the following, we describe the flame structures that were observed in our sub-millimetre burner for a variety of inlet mixture strengths (the inlet molar ratio of fuel to oxidizer normalized by the stoichiometric molar ratios) and inlet flow rates. With stoichiometric inlet flow rates of 100 sccm  $CH_4$  and 200 sccm  $O_2$  ( $Re_{est} = 67$ ), the mixture in the burner was ignited. Initially, a continuous, smooth, laminar diffusion flame formed in the mixing layer along the channel length between the fuel and oxidizer streams. The methane/air burner exit flame described above was also present. As the burner walls heated up, the diffusion flame inside the burner developed a distinct cellular structure along its length, before collapsing into three isolated flame cell structures of the type that are described below. Unless noted otherwise, this equilibrium structure serves as the initial conditions from which all the cases described below were obtained. We consider two cases: the methane/air flame at the burner exit is either present or quenched.

#### 3.1 Diffusion flame cone extinguished

In the first set of experiments, the burner was first ignited as described above. When the temperature on the outside wall had equilibrated (as determined by thermocouples placed along the centre of the top 16 mm of one of the 5 mm wide burner walls above the manifold), the methane/air burner exit flame was extinguished by gently blowing across the top of the burner. Thereafter the methane/oxygen supply flow rates and/or the initial mixture strengths were varied and the luminosity images recorded. The equilibrium combustion structure that arises for flow rates of 100 sccm  $CH_4$  and 200 sccm  $O_2$  is shown in figure 3(c). As discussed above, given the burner configuration shown in figure 1, it would be reasonable to expect that combustion should occur via a single, continuous laminar diffusion flame in the mixing layer formed between the methane and oxygen streams. Instead, the luminosity images show the

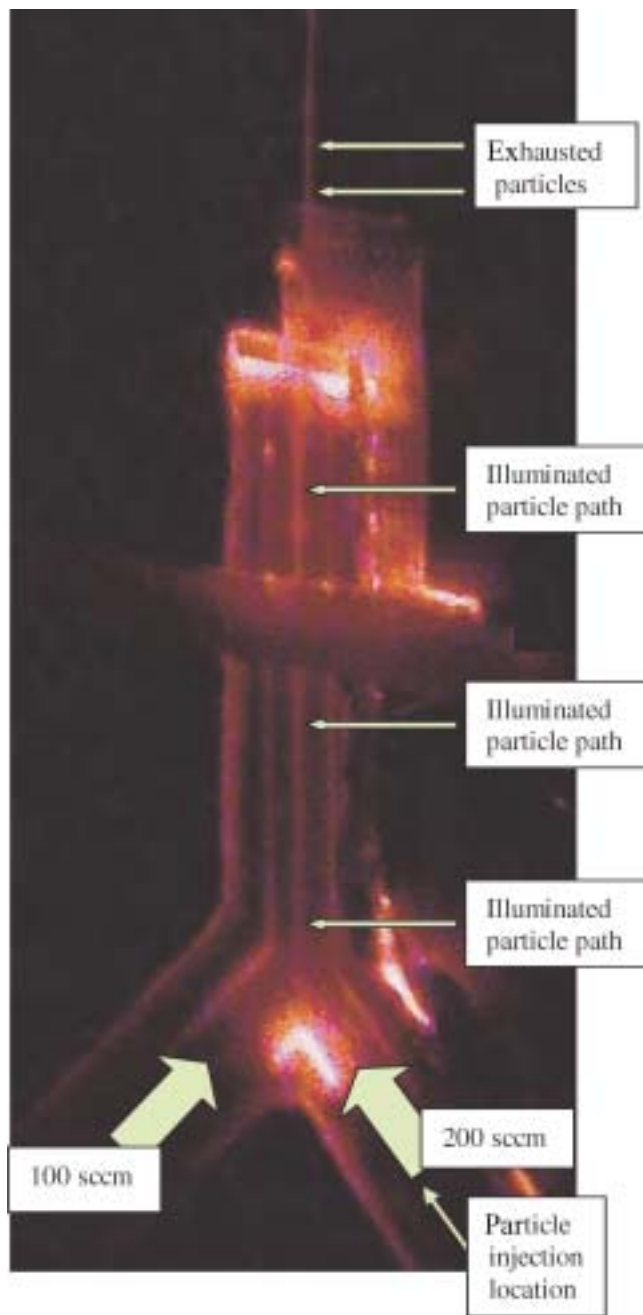


Figure 2. Cold flow streamline pattern obtained by laser illumination of fine smoke particles for injection rates of 200 sccm in the right side of the Y inlet shown in figure 1(a) and 100 sccm in the left ( $Re \sim 86$  in the burner channel, based on the smaller dimension). The particles are introduced into the inlet stream near the inside wall of the right (200 sccm) Y inlet, so that the streamline pattern represents the flow near the mixing layer between the two inlet streams.

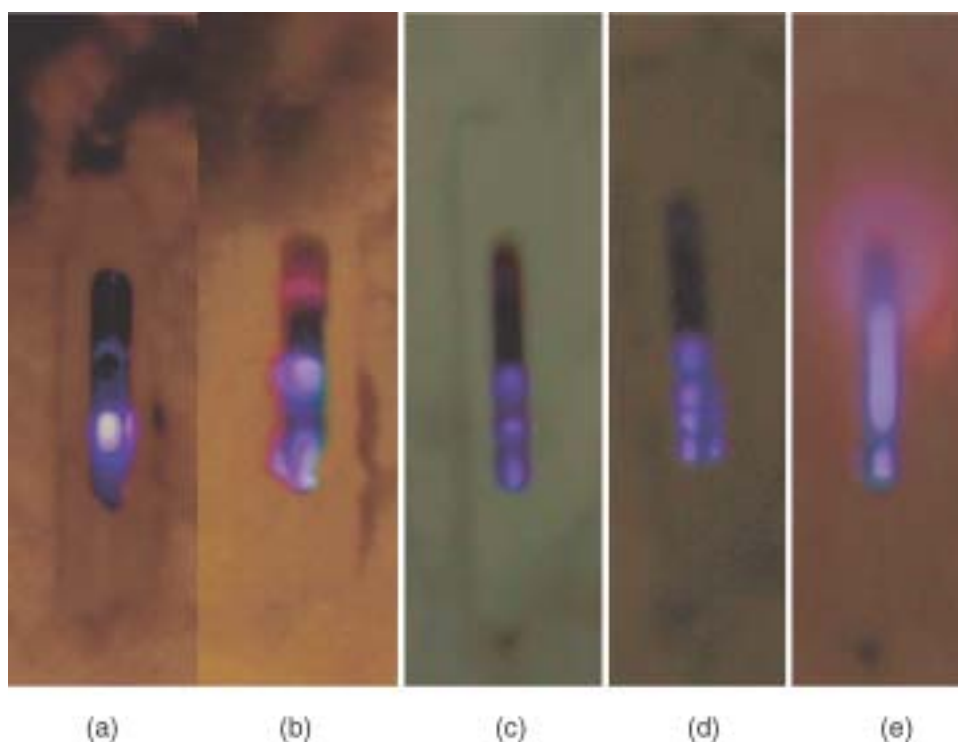


Figure 3. Chemiluminescent emission from: (a) one flame cell formed with 29 sccm  $\text{CH}_4$  and 171 sccm  $\text{O}_2$ ; (b) two flame cells for 67 sccm  $\text{CH}_4$  and 266 sccm  $\text{O}_2$ ; (c) three flame cells for 100 sccm  $\text{CH}_4$  and 200 sccm  $\text{O}_2$ ; (d) four flame cells for 100 sccm  $\text{CH}_4$  and 130 sccm  $\text{O}_2$ . The smaller blue colourations slightly to the right of the more prominent flames in (d) are reflections of the true flames on the burner wall. The red patch observed in (b) is from the glowing alumina. Variations in the background colour are associated with variations in the room lighting. (e) The laminar diffusion flame structure atop a single flame cell for 65 sccm  $\text{CH}_4$  and 150 sccm of  $\text{O}_2$ . A methane/air diffusion flame can also be observed at the exit to the burner.

presence of three isolated reaction zone structures—which we denote as flame cells—that extend along the length of the burner in the direction of the flow.

The precise structure of the flame cells inside the burner is hard to ascertain due to the restricted viewing angle. However, they appear to be characterized by strong chemiluminescent emission in small regions approximately 2–3 mm in length, and almost appear to touch the burner walls separated by 0.75 mm. By adjusting the flow rates, a flame cell could be made to approach the top of the burner, whereupon it appeared to have a tribrachial structure with a very short diffusion tail. In fact, these are reminiscent of some of the edge-flame structures observed in non-premixed systems with heat losses [25, 26] in which the leading-edge structure is more able to withstand the heat losses than the trailing diffusion flame. The flame cell at the base of the burner appears to be stretched lengthwise in comparison to the top two cells (figure 3(c)), presumably due to the flame stretch that is induced by the straining flow when the two inlet supply jets initially collide at the base of the burner (figure 1). These multiple burning structures were extremely stable and were present during continuous operation of the burner over a period of several days. Most importantly, it is clear that homogeneous combustion is occurring inside the burner.

Figure 3 shows the variety of other structures that were observed for various  $\text{CH}_4/\text{O}_2$  inlet flow rates and initial mixture strengths. We found conditions for which one, two, three or four flame cells may exist in the microburner channel, typical examples of which are shown in

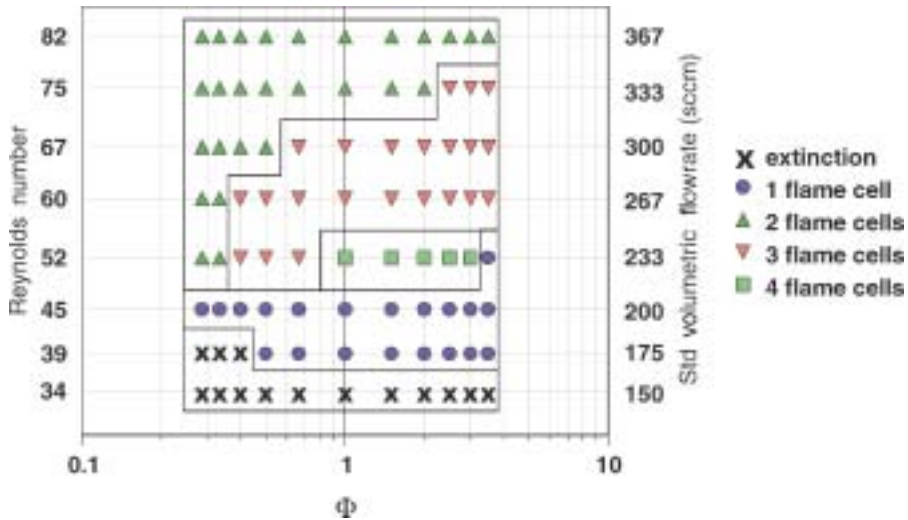


Figure 4. Flame structure map (total flow rate against initial mixture strength) of the combustion structure observed inside the burner with the exit methane/air flame absent. The designations 1, 2, 3 and 4 flame cells refer to structures similar to those shown in figures 3(a)–(d), respectively. The symbol X refers to conditions where combustion cannot be sustained in the burner. Note that inlet velocity ( $\text{cm s}^{-1}$ ) based on  $25^\circ\text{C}$  gases can be determined by multiplying the standard volumetric flowrate by the factor 0.485.

figures 3(a)–(d). Importantly, changes in the inlet flow rates and/or initial mixture strengths led to changes in the position of the flame cells within the burner. This migration allows us to eliminate one potential source for the existence of the isolated flame cells, i.e. the failure of the burner manufacture process to uniformly reduce or eliminate the action of chemical quenching at isolated spots on the burner walls.

Figure 4 shows a flame structure regime map summary of the type of burning structures observed inside the burner for various initial mixture strengths  $\Phi$  ( $0.29 < \Phi < 3.5$ ) and total flow rates  $u_i$  ( $150 < u < 367$ ;  $34 \leq Re_{\text{est}} \leq 82$  where  $u_i$  is the combined inlet flow rate of  $\text{CH}_4$  (sccm) and  $\text{O}_2$  (sccm)). The flame structure regime map was constructed by first igniting and equilibrating the burner as described above with flow rates of 100 sccm  $\text{CH}_4$  and 200 sccm  $\text{O}_2$ . The flow rates were then adjusted to the desired level with the methane/air flame at the burner exit remaining. The methane/air flame was then extinguished if it had not extinguished naturally during the change in flow conditions. Conditions inside the burner were allowed to equilibrate once again, and the nature of the combustion field inside the burner was recorded. For the higher total flow rates in the range studied, e.g. for  $u_i = 367$  sccm ( $Re_{\text{est}} = 82$ ), where the convective gas velocities were the highest, and the shortest burner gas residence time, two flame cells were noted inside the burner regardless of the initial mixture strength (figure 4). The flame cells observed at the higher flow rates tended to be more elongated than their counterparts at the lower total flow rates. For fuel-lean mixtures ( $\Phi < 1$ ) and  $u_i = 367$  sccm, the second flame cell extended close to the burner sidewall on the methane inlet side, and also had a faint luminosity emission. At increased  $\Phi$ , the second flame cell first moved toward the centre of the burner, and ultimately positioned itself on the oxidizer side of the burner; it also moved lower in the burner.

With lower total flow rates, and the range of  $\Phi$  considered, the number of flame cells that may be observed increases as the initial mixture strength increases. For example, for  $u_i = 233$  sccm ( $Re_{\text{est}} = 52$ ), two flame cells were present for  $\Phi < 0.33$ , three flame cells were present for  $0.4 < \Phi < 0.67$  and four flame cells were present for  $1 < \Phi < 3$ . Figure 3(d) shows the luminous emission from the four flame cells that were present for 130 sccm  $\text{O}_2$  and

100 sccm CH<sub>4</sub>. It is reasonable to surmise that more flame cells will appear as the quantity of methane fed into the burner increases, whilst not changing the overall convective timescale in the channel based on the average inlet flow rate. However, it is also interesting to note that for initial mixture strengths of  $\Phi = 0.5$  and  $\Phi = 3$ , where the total amount of methane that may be consumed in the burner is the same, we observed three cells for  $\Phi = 0.5$  and four cells for  $\Phi = 3$ . This could be due to a number of factors. For example, for a given  $\Phi$ , the net ratio of inlet flow rates  $u_{O_2}/u_{CH_4}$  is  $2/\Phi$ . Consequently the  $u_{O_2}/u_{CH_4}$  ratio for a fuel-lean mixture ( $\Phi < 1$ ) will be higher than for the corresponding fuel-rich mixture with an initial mixture strength  $2/\Phi - 1$  for which the same amount of methane could be consumed. Thus the flame may experience more heat loss due to the proximity of the mixing layer to the relevant burner sidewall in the case for  $\Phi = 0.5$  relative to that for  $\Phi = 3$ .

For sufficiently low total flow rates, the reaction is sufficiently weak that only a single flame cell existed at the base of the burner; this flame cell was ultimately extinguished as the total flow rate decreased further.

The variation in the burner channel combustion structure with the methane/air exit flame absent, the initial mixture strength fixed and the total flow rate varied is as follows. For very fuel-lean mixtures, the two flame cells present at higher flow rates, are reduced to one at intermediate flow rates, which in turn quenches at the lower flow rates. For intermediate initial mixture strengths, the two elongated flame cells, associated with the high convective flow rates in the channel, first increase in number as the total flow rate is reduced, i.e. as the ratio of the characteristic diffusion timescale to the convection timescale in the channel increases. For  $u_i = 1$ , there were two flame cells present for  $u_i = 367$  sccm ( $Re_{est} = 82$ ), but four flame cells were present for  $u_i = 233$  sccm. Once the total flow rate reached a sufficiently low value, the number of flame cells began to drop. There was a single flame cell at the base of the burner for  $\Phi = 1$  and  $u_i = 200$  sccm ( $Re_{est} = 45$ ).

### 3.2 Diffusion flame cone lit

Some new flame structures in addition to those described above may be obtained inside the burner if the methane/air flame at the burner exit is not extinguished when studying the flame patterns at set flow rates and initial mixture strengths. Clearly though, the presence of any reaction external to the microburner is unacceptable for most practical applications.

At flow rates of 100 sccm CH<sub>4</sub> and 200 sccm O<sub>2</sub>, there were three flame cells in the temperature-equilibrated burner in addition to the diffusion flame at the burner exit. When the O<sub>2</sub> flow rate was decreased (maintaining the methane flow rate at 100 sccm) the top two flame cells were observed to move down the burner. However, with the methane/air flame present and with a flow rate of 140 sccm O<sub>2</sub> ( $Re_{est} = 54$ ), a fourth flame cell was ignited just below the exit to the burner. Clearly the methane/air flame is acting as the ignition source, since a fourth cell is not ignited if the flame is absent. With further decreases in the O<sub>2</sub> flow rate, the uppermost three flame cells continued to move lower down the burner, while the average lengthwise spacing between them also decreased. At even lower O<sub>2</sub> flow rates, some interesting dynamic instabilities of the flame cells were observed. For instance, when the O<sub>2</sub> flow rate was reduced to 117 sccm ( $Re_{est} = 49$ ), the top three flame cells coalesced into a continuous laminar diffusion flame with a distinct cellular structure. The bottom flame cell persisted. For still lower O<sub>2</sub> feed rates, the laminar flame began to lose its cellular structure. A chemiluminescent image of a smooth laminar flame above a single flame cell, which we call the ‘exclamation mark’ structure, is shown in figure 3(e). The presence of the single flame cell probably results from the strained flow at the base of the burner caused by the angled inlet streams, where the magnitude of the strain rate at the base of the burner appears to be sufficient to quench the trailing diffusion flame just downstream of the leading edge of the first flame

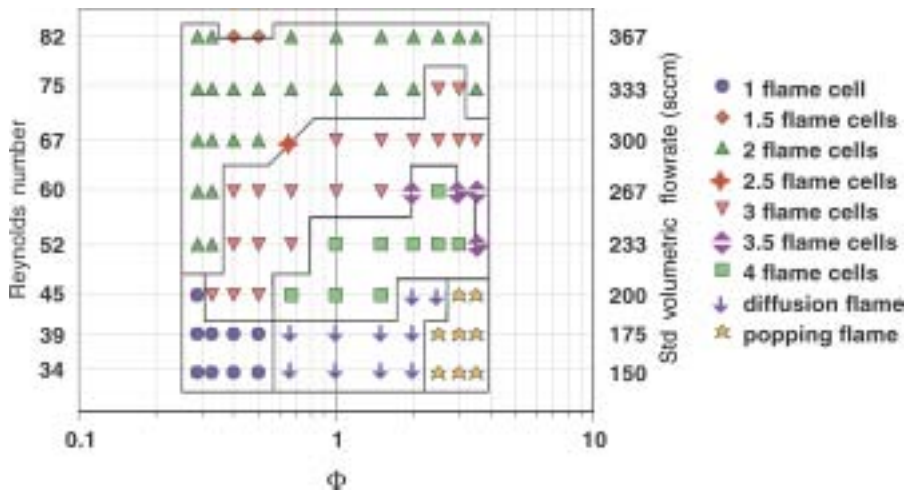


Figure 5. As in figure 4, except with the exit methane/air flame present. The ‘diffusion flame’ points indicate the presence of the exclamation mark structure similar to that seen in figure 3(e), while ‘popping’ indicates a pulsating instability of the diffusion flame. The notation 1.5, 2.5 and 3.5 flame cells refer to the cases where another flame cell is observed near the top of the burner but the flame cell is not completely within the burner. Note that inlet velocity ( $\text{cm s}^{-1}$ ) based on  $25^\circ\text{C}$  gases can be determined by multiplying the standard volumetric flow rate by the factor 0.485.

cell. Subsequently as the strain rate decreases further up the channel, above the inlet streams, the diffusion flame can exist once again.

With a flow rate of 76 sccm  $\text{O}_2$  ( $Re_{\text{est}} = 39$ ), the laminar diffusion flame portion of the exclamation mark structure underwent an observable pulsation in which the leading edge of the diffusion flame pulsed up and down the channel. The bottom ball appeared to remain unaffected. With a flow rate of 58 sccm  $\text{O}_2$  ( $Re_{\text{est}} = 35$ ), the pulsation comprised two events—a large-amplitude signal with a frequency of 36 Hz (associated with a flickering of the burner exit methane/air flame in addition to the pulsation of the diffusion flame in the burner) and a lower amplitude signal with a frequency of 55 Hz (associated with pulsation of the internal burner flame alone). With a further decrease in the  $\text{O}_2$  flow rate, the pulsating laminar flame portion of the exclamation mark structure extinguished, and a single ball located at the bottom of the burner remained. Interestingly, the pulsation instabilities reported here did not occur if the total combined flow rates were too high. For example, for 150 sccm  $\text{CH}_4$  and 68 sccm  $\text{O}_2$  ( $Re_{\text{est}} = 49$ ), the burner methane/oxygen diffusion flame that was present simply extinguished at sufficiently low flow rates of  $\text{O}_2$ , but did so without entering a prior oscillating phase.

Figure 5 shows the flame structure map of the burning structures observed inside the burner for various equivalence ratios ( $0.29 \leq \Phi \leq 3.5$ ) and total flow rates ( $150 \leq u \leq 367$ ;  $34 \leq Re_{\text{est}} \leq 82$ ) when the exit methane/air flame was not extinguished manually. They were obtained as before by first allowing the burner state to equilibrate with flow rates of 100 sccm  $\text{CH}_4$  and 200 sccm  $\text{O}_2$ . The flow rates were then adjusted to the desired level, the burner state again equilibrated, and the flame structure observations recorded. For the higher total flow rates, the observed structures and variations were similar to those shown in figure 4 with the methane/air flame absent. The major differences occurred at the lower flow rates, with the appearance of additional combustion structures within the microburner that did not occur when the exit methane/air flame was absent. Moreover, combustion inside in the channel was supported in regimes where no combustion was possible when the methane/air flame was absent.

For example, when  $u_1 = 200$  sccm ( $Re_{\text{est}} = 45$ ), there was a transition from one, to three to four cells as  $\Phi$  increased. There was then a transition from the four flame cells at  $\Phi = 1.5$  to

the exclamation mark structure at  $\Phi = 2$ . Further increases in  $\Phi$  into the fuel-rich regime then led to a pulsating instability of the diffusion flame inside the burner. When the methane/air exit flame was absent for all the same inlet conditions, one flame cell was observed in all cases. The transition values of the initial mixture strength at which the exclamation mark structure and the pulsating instability occurred decreased as the total injection flow rate was lowered. For the low flow rates, the exclamation mark structure may occur in fuel-lean conditions, but the pulsating instability was found to occur only for fuel-rich ( $\Phi > 1$ ) mixtures. For sufficiently low total flow rates, no combustion can occur inside the burner, in spite of the presence of the exit methane/air flame. On the other hand, for a decrease in the total flow rate at fixed initial mixture strength sufficiently close to stoichiometric, there was a transition from four cells to the exclamation mark structure, and then to a single flame cell without any pulsating instability. For sufficiently fuel-rich inlet conditions, the diffusion flame associated with the exclamation mark structure underwent a pulsating instability as the total flow rate decreased, before the diffusion flame extinguished leaving only a single flame cell at the base of the burner. Finally, for very fuel-rich mixtures, there was a transition from four stable cells straight to the pulsating instability of the exclamation mark instability, apparently without passing through the intermediate stable exclamation mark structure.

#### 4. Discussion

We have identified a form of methane–oxygen cellular diffusion flame instability in a microburner with a 0.75 mm channel gap that appears to be unique to confined microscale combustion. Gas-phase combustion was enabled in the microburner by chemically treating and annealing the vessel walls. The observed flame cells appeared to have a tribrachial flame structure with a short diffusion flame tail, somewhat reminiscent of the edge-flame structures observed in non-premixed systems with heat losses [25, 26]. The flame cells occurred along the length of combustion channel, parallel, not perpendicular to the flow direction. Although cellular diffusion flame instabilities have been examined many times previously (e.g. [21–24]), they are normally associated with effective low Lewis number mixtures, and in near combustion limit conditions. In contrast, the flame cells observed in the microburner occurred here in a methane–oxygen system, and for a wide variety of inlet flow rates and initial mixture strengths. The number of cells observed in the present microburner configuration varied between one and four depending on the inlet flow rates and initial mixture strengths of the methane and oxygen supply gases, and these dependencies have been characterized in the current paper. In addition, when a methane/air flame is present at the burner exit, arising as a result of unconsumed methane in the exhaust gases, combustion inside in the channel can be supported in regimes where no combustion occurs when the methane/air flame is absent. Moreover, in some of these cases, the flame cells were observed to collapse into a continuous laminar diffusion flame, termed an exclamation mark structure. In fuel-rich and near-quenching conditions, this continuous laminar flame may undergo a pulsating instability along the burner channel.

Based on the variations shown in figures 4 and 5, a basic mechanism underlying the formation of the isolated flame cells can be postulated, although the exact details are likely to be significantly influenced by many important issues such as heat transfer within the burner walls, as discussed below. The methane and oxygen inlet streams collide and generate a mixing layer above the splitter plate extending the length of the burner combustion channel (figure 2). A premixed edge-flame-like structure can then exist at a relevant point in the mixing layer above the splitter plate [25]. Without the near-wall confinement present in the microburner, we would then expect a laminar diffusion flame to exist behind the premixed edge. However, in the presence of conductive heat losses to the burner walls, in addition to convective heat

losses from gas flow through the channel, it appears that the trailing diffusion flame cannot be sustained. As mentioned above, this is a characteristic of non-premixed edge-flame propagation in the presence of heat losses. Subsequently, methane and oxygen can then diffuse into the mixing layer behind the first cell, until an additional leading-edge structure can be supported. For instance, figures 4 and 5 indicate that for a fixed initial mixture strength, the number of cells that appear increases as the total flow rate decreases, or the residence time of the gases in the burner is increased, allowing more time for inter-flame cell mixing of gases. This occurs until the mixture becomes sufficiently weak that only one cell can be sustained at the base of the burner. In summary, figures 4 and 5 indicate that the number of flame cells is determined by the ratio of the rate of convective gas flow axially along the burner to the rate of radial viscous diffusion of gases between the flame cells in comparison to the relative reactivity of the fuel/oxidizer reaction. This effect is thus highly dependent on the relative mass and thermal diffusivities of the inlet gases and their characteristic rate of reaction. Work is currently ongoing to determine the dependence of the flame cell structure on the type of fuel and inert diluent used in the microburner.

Of particular interest with regard to the mechanisms behind the flame cell formation is the heat distribution within the burner for a given flame cell configuration, especially with regard to the axial heat flow within and along the burner walls that may preheat the inlet gas before combustion. Work is currently underway to determine the thermal distributions within the burner walls and their relation to flame stability. We have obtained some preliminary insights by obtaining approximate distributions of the thermal variations on the outside burner walls. These were obtained by equally spacing seven thermocouples along the centre of the top 16 mm of one of the 5 mm wide combustion channel walls. An example of these measurements is shown in figure 6, where the total flow rate was fixed at 300 sccm ( $Re_{est} = 67$ ) and the initial mixture strength was varied. The readings were obtained with the burner assembly placed in a fume cupboard. For fuel-lean mixtures, two flame cells were present in the microburner. The appearance of a third flame cell near the top of the burner as  $\Phi$  increased is clearly reflected on the outside burner wall temperature, as is the migration of the flame cell down into the burner channel with further increases in  $\Phi$ . Around the position of a flame cell, there is a typical local temperature rise of 85°C in the outside burner wall temperature. However, it would appear from these readings that the wall temperatures were fairly uniformly heated, and it is likely that the inlet gases were being heated to some extent by axial heat transfer along the burner walls. Perhaps more importantly, it is also interesting to note that the flame cells instantaneously moved to new positions in the burner on changing the inlet flow rate and/or initial mixture strength. The temperature on the outside of the burner walls then adjusted to the new position of the flame cells over a much longer period. In this sense, it is likely that the mechanisms underlying the formation of the flame cells are not too dependent on the heat distribution within the burner walls, but perhaps depend more on the heat losses that occur to the surrounding atmosphere. Finally, the alumina used in the burner construction also has an interesting property, namely that its thermal conductivity decreases sixfold from 36 Wm<sup>-1</sup> K<sup>-1</sup> at  $T = 300$  K to 5.59 Wm<sup>-1</sup> K<sup>-1</sup> at  $T = 1800$  K [27]; this may also influence heat transfer along the burner walls where flame cells are present and where they are not. In any case, further work on the temperature variations within the microburner walls is ongoing.

Additional visualization experiments are also planned to ascertain the possible role of any thermal-diffusive or hydrodynamic flow instabilities in the burner, such as those that may arise from Kelvin–Helmholtz instabilities, boundary layer separation from the burner walls, or density or viscosity changes under combustion. The cold flow experiments discussed earlier (figure 2) indicate that the underlying flow in the burner appears to be very laminar.

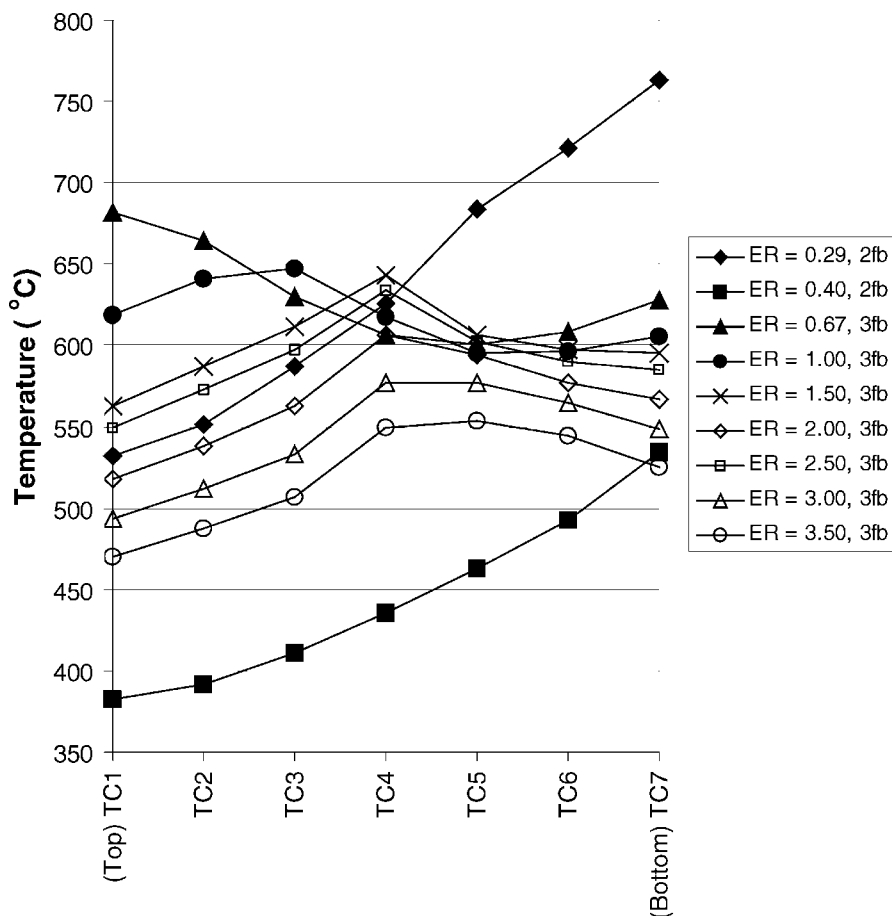


Figure 6. Temperature profiles of the outside of the burner wall for a range of methane/oxygen equivalence ratios (all at a total inlet flow rate of 300 sccm) taken from seven thermocouples placed equidistantly along the centreline of the top 16 mm of one of the 5 mm wide burner walls. The exit methane/air flame was absent. The symbol TC1 refers to thermocouple placed nearest to the burner exit. The symbols 2fb and 3fb refer to the presence of two or three flame cells, respectively.

In order to further clarify many of the issues underlying the formation of the microburner flame cells, a series of experiments are currently in progress that will also examine the effect of the channel breadth (currently 5 mm), its width (in the range of 0.25 mm to 2 mm) and length (in the range 20–80 mm). We are also investigating the effect of the fuel and oxidizer properties, primarily the role of the Lewis number, on the generation of flame cells. Finally, we are also currently conducting a series of two- and three-dimensional numerical computations based on the burner geometry and properties to further investigate the structure and dynamics of the flame cells, including identifying the possible role of intermediate reaction species through their relative mass and thermal diffusivity properties.

In conclusion, we have identified a new flame structure relevant to microscale combustion; additional modelling is required in order to fully understand its structure. While the appearance of flame cells for the methane–oxygen system is of much interest from a fundamental flame structure viewpoint, they do in fact represent an undesirable mode of combustion in terms of practical microburner operation, since the degree of methane conversion inside the burner is small (typically estimated to be <40% from gas chromatography measurements of exhaust gases).

## Acknowledgements

This work was supported by the Department of Defense Multidisciplinary University Research Initiative (MURI) program administered by the Army Research Office under contract DAAD19-01-1-0582. Any opinions, findings, conclusions or recommendations expressed in this publication are those of the authors and do not necessarily reflect the views of the Department of Defense or the Army Research Office. RIM and MAS hold a US patent on the microburner design [28]. MS received additional support from the AFOSR. The authors are very grateful to B. Balasubramaniam for his assistance with the cold flow visualization results. Correspondence and requests for materials should be addressed to RIM (email: r-masel@uiuc.edu).

## References

- [1] Davy, H., 1814, An account of an invention for giving light in explosive mixtures of fire-damp in coal mines, by consuming the fire-damp. *Philosophical Transactions*, **23**, 114.
- [2] Lewis, B. and von Elbe, G., 1987, *Combustion, Flames and Explosions of Gases* (New York: Academic).
- [3] Kuo, K.K., 1986, *Principles of Combustion* (New York: Wiley).
- [4] Fernandez-Pello, A.C., Pisano, A.P., Fu, K., Walther, D.C., Knobloch, A., Martinez, F., Senesky, M., Jones, D., Stoldt, C. and Heppner, J., 2002, MEMS rotary engine power system. Paper presented at the International Workshop on Power MEMS (Power MEMS 2002) Ibaraki, Japan, 12–13 November.
- [5] Fu, K., Knobloch, A., Martinez, F., Walther, D.C., Fernandez-Pello, A.C. Pisano, A.P., and Liepmann, D., 2001, Design and fabrication of a silicon-based MEMS rotary engine. Paper presented at the 2001 International Mechanical Engineering Congress and Exposition (IMECE), New York, 11–16 November.
- [6] Fu, K., Knobloch, A., Martinez, F., Walther, D.C., Fernandez-Pello, A.C., Pisano, A.P., Liepmann, D., Miyaska, K. and Maruta, K., 2001, Design and experimental results of small-scale rotary engines. Paper presented at the 2001 International Mechanical Engineering Congress and Exposition (IMECE), New York, 11–16 November.
- [7] Lee, D.H., Park, D.E., Yoon, J.B., Kwon, S. and Yoon, E., 2002, Fabrication and test of a MEMS combustor and reciprocating device. *Journal of Micromechanics and Microengineering*, **12**, 26–34.
- [8] Mehra, A., Zhang, X., Ayon, A.A., Waitz, I.A., Schmidt, M.A. and Spadaccini, C.M., 2002, A six-wafer combustion system for a silicon micro gas turbine engine. *Journal of Micromechanical Systems*, **9**, 517–527.
- [9] Fernandez-Pello, A.C., 2002, Micropower generation using combustion: issues and approaches. *Proceedings of the Combustion Institute*, **29**, 883–899.
- [10] Peterson, R.B. and Hatfield, J.M., 2001, A catalytically sustained microcombustor burning propane. *Micro-Electro-Mechanical Systems*, **3**, 861–865.
- [11] Sitzki, L., Borer, K., Wussow, S., Schuster, E., Maruta, K., Ronney, P. and Cohen, A., 2001, Combustion in microscale heat-recirculating burners. Paper presented at AIAA-2001-1087, 39th AIAA Space Sciences and Exhibit, Reno, NV, 8–11 January.
- [12] Sitzki, L., Borer, K., Schuster, E., Ronney, P. and Wussow, S., 2001, Combustion in microscale heat-recirculating burners. Paper presented at the 3rd Asia-Pacific Conference on Combustion, Seoul, Korea, 24–27 June.
- [13] Loffler, D.G. and Schmidt, L.D., 1976, Kinetics of ammonia decomposition on polycrystalline platinum. *Journal of Catalysis*, **41**, 440–454.
- [14] Loffler, D.G. and Schmidt, L.D., 1976, Kinetics of NH<sub>3</sub> decomposition on single crystal planes of platinum. *Surface Science*, **59**, 195–204.
- [15] Jensen, C.D., 2000, The dependence of flame/wall interactions on the composition of the walls for determining the material composition of a micro-combustor. MSc thesis, University of Illinois at Urbana-Champaign.
- [16] Ronney, P.D., Wu, M.S., Pearlman, H.G. and Weiland, K.J., 1998, Structure of flame balls at low Lewis number (SOFBALL): preliminary results from the STS-83 space flight experiments. *AIAA Journal*, **36**, 1361–1368.
- [17] Kaiser, C., Liu, J.B. and Ronney, P.D., 2000, Diffusive thermal instability of counterflow flames at low Lewis numbers. Paper presented at AIAA 2000-0576 38th Aerospace Sciences Meeting and Exhibition, Reno, NV, 11–14 January.
- [18] Buckmaster, J.D., Joulin, G. and Ronney, P.D., 1991, Effects of heat loss on the structure and stability of flame balls. *Combustion and Flame*, **79**, 381–392.
- [19] Buckmaster, J.D., Joulin, G. and Ronney, P.D., 1991, Structure and stability of non-adiabatic flames balls: II. Effects of far-field losses. *Combustion and Flame*, **84**, 411–422.
- [20] Short, M., Buckmaster, J. and Kochevets, S., 2001, Edge-flames and sublimit hydrogen combustion. *Combustion and Flames*, **125**, 893–905.
- [21] Dongworth, M.R. and Melvin, A., 1976, The transition to instability in a steady hydrogen–oxygen diffusion flame. *Combustion Science and Technology*, **14**, 177–182.

- [22] Chen, R., Mitchell, G.B. and Ronney, P.D., 1992, Diffusive-thermal instability and flame extinction in non-premixed combustion. *Proceedings of the Combustion Institute*, **24**, 213–221.
- [23] Kim, J.S., 1997, Linear analysis of diffusional-thermal instability in diffusion flames with Lewis numbers close to unity. *Combustion Theory and Modelling*, **1**, 13–40.
- [24] Cheatham, S. and Matalon, M., 2000, A general asymptotic theory of diffusion flames with applications to cellular instability. *Journal of Fluid Mechanics*, **414**, 105–144.
- [25] Kurdyumov, V.N. and Matalon, M., 2002, Radiation losses as a driving mechanism for flame oscillations. *Proceedings of the Combustion Institute*, **29**, 45–52.
- [26] Daou, R., Daou, J. and Dold, J.W., 2002, Effect of volumetric heat loss on triple-flame propagation. *Proceedings of the Combustion Institute*, **29**, 1559–1564.
- [27] Touloukian, Y.S., Powell, R.W., Ho, C.Y. and Klemens, P.G., 1970, *Thermal Conductivity, Thermophysical Properties of Matter*, Vols. 1 & 2 (New York: Plenum).
- [28] Masel, R.I. and Shannon, M.A., 2001, Microcombustor having submillimeter critical dimensions. US Patent 6193501.